



HAL
open science

Varying growth behavior of redox-sensitive nanoparticles on 1:1 and 2:1 clay surfaces: mechanistic insights on preferential toxic ions removal in mono, co and multi-metal contaminated waters

Nitin Khandelwal, Nisha Singh, Ekta Tiwari, Remi Marsac, Dieter Schild, Thorsten Schäfer, Gopala Krishna Darbha

► To cite this version:

Nitin Khandelwal, Nisha Singh, Ekta Tiwari, Remi Marsac, Dieter Schild, et al.. Varying growth behavior of redox-sensitive nanoparticles on 1:1 and 2:1 clay surfaces: mechanistic insights on preferential toxic ions removal in mono, co and multi-metal contaminated waters. *Chemical Engineering Journal*, 2023, 461, pp.141883. 10.1016/j.cej.2023.141883 . insu-03997222

HAL Id: insu-03997222

<https://insu.hal.science/insu-03997222v1>

Submitted on 20 Feb 2023

HAL is a multi-disciplinary open access archive for the deposit and dissemination of scientific research documents, whether they are published or not. The documents may come from teaching and research institutions in France or abroad, or from public or private research centers.

L'archive ouverte pluridisciplinaire **HAL**, est destinée au dépôt et à la diffusion de documents scientifiques de niveau recherche, publiés ou non, émanant des établissements d'enseignement et de recherche français ou étrangers, des laboratoires publics ou privés.

Journal Pre-proofs

Varying growth behavior of redox-sensitive nanoparticles on 1:1 and 2:1 clay surfaces: mechanistic insights on preferential toxic ions removal in mono, co and multi-metal contaminated waters

Nitin Khandelwal, Nisha Singh, Ekta Tiwari, Remi Marsac, Dieter Schild, Thorsten Schäfer, Gopala Krishna Darbha

PII: S1385-8947(23)00614-9
DOI: <https://doi.org/10.1016/j.cej.2023.141883>
Reference: CEJ 141883

To appear in: *Chemical Engineering Journal*

Received Date: 21 November 2022
Revised Date: 16 January 2023
Accepted Date: 11 February 2023

Please cite this article as: N. Khandelwal, N. Singh, E. Tiwari, R. Marsac, D. Schild, T. Schäfer, G. Krishna Darbha, Varying growth behavior of redox-sensitive nanoparticles on 1:1 and 2:1 clay surfaces: mechanistic insights on preferential toxic ions removal in mono, co and multi-metal contaminated waters, *Chemical Engineering Journal* (2023), doi: <https://doi.org/10.1016/j.cej.2023.141883>

This is a PDF file of an article that has undergone enhancements after acceptance, such as the addition of a cover page and metadata, and formatting for readability, but it is not yet the definitive version of record. This version will undergo additional copyediting, typesetting and review before it is published in its final form, but we are providing this version to give early visibility of the article. Please note that, during the production process, errors may be discovered which could affect the content, and all legal disclaimers that apply to the journal pertain.

© 2023 Published by Elsevier B.V.



Varying growth behavior of redox-sensitive nanoparticles on 1:1 and 2:1 clay surfaces: mechanistic insights on preferential toxic ions removal in mono, co and multi-metal contaminated waters

Nitin Khandelwal^{a,b}, Nisha Singh^{a,c}, Ekta Tiwari^{a,d}, Remi Marsac^e, Dieter Schild^f, Thorsten Schäfer^g, and Gopala Krishna Darbha^{a,h,*}

^aEnvironmental Nanoscience Laboratory, Department of Earth Sciences, Indian Institute of Science Education and Research (IISER) Kolkata, Mohanpur, West Bengal 741246, India

^bEnvironmental Engineering Laboratory, Department of Civil Engineering, McGill University, Montreal H3A 0C3, Quebec, Canada

^cJapan Agency for Marine-Earth Science and Technology (JAMSTEC), 2-15 Natsushima, Yokosuka, Kanagawa, 237-0061, Japan

^dNatural Resources Management & Environmental Sciences, College of Agriculture, Food & Environmental Sciences, California Polytechnic State University, CA, 93401, USA

^eUniversity of Rennes1, CNRS, Géosciences Rennes, UMR 6118, 35000 Rennes, France.

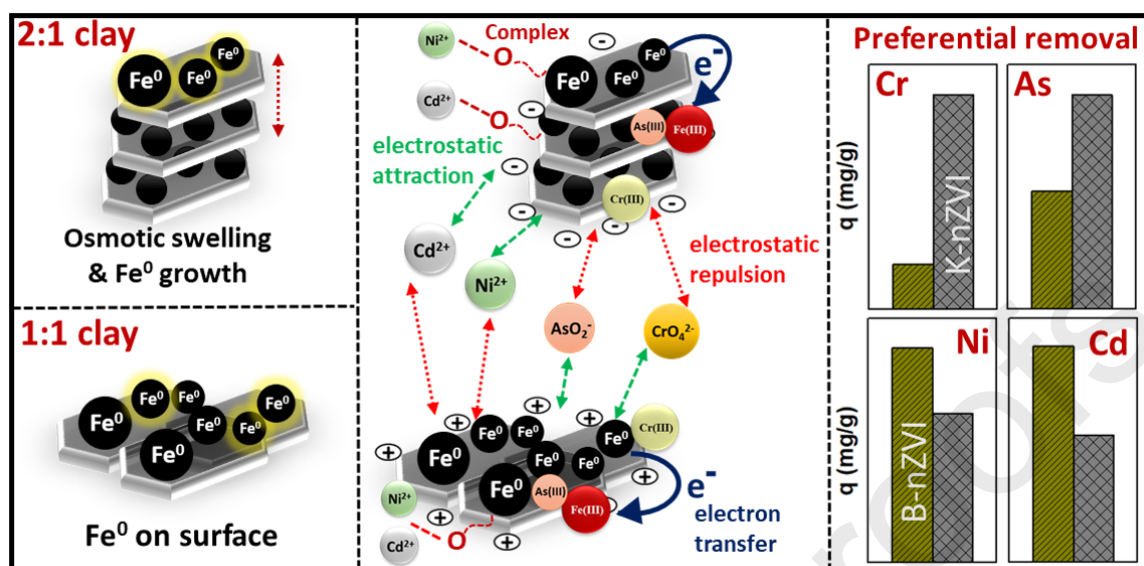
^fKarlsruhe Institute of Technology (KIT), Institute for Nuclear Waste Disposal, Hermann-von-Helmholtz-Platz 1, 76344, Eggenstein-Leopoldshafen, Germany

^gInstitute of Geosciences, Applied Geology, Friedrich-Schiller-University Jena, Burgweg 11, D-07749, Jena, Germany

^hCentre for Climate and Environmental Studies, Indian Institute of Science Education and Research (IISER) Kolkata, Mohanpur, West Bengal 741246, India

*Corresponding author: Gopala Krishna Darbha, Email- gkdarbha@gmail.com, gkdarbha80@yahoo.com Tel: (+91)- 9849626082

Graphical abstract



Highlights

- Dominant interlayer growth of Fe⁰ NPs on 2:1 bentonite form B-nZVI (-ve charge)
- Non-swelling 1:1 kaolinite with surface coverage of Fe⁰ NPs led to K-nZVI (+ve)
- Preferential sorption of toxic cations on B-nZVI (63 mg/g) than K-nZVI (33 mg/g)
- Higher removal of oxy-anions with K-nZVI (248 mg/g) than B-nZVI (149 mg/g)
- Removal mechanisms were redox transformation, complexation and co-precipitation

Abstract

In the current study, contrasting growth behaviour of redox sensitive Fe⁰ nanoparticles (nZVI) was observed on different clay surfaces i.e., 1:1 non-swelling kaolinite (K-nZVI) and 2:1 swelling bentonite (B-nZVI). Osmotic swelling of bentonite led to Fe⁰ nucleation and growth of 5-7 nm size particles in the broadened interlayer spaces. B-nZVI had negative zeta potential due to the domination of the surface charge of bentonite clay. Whereas kaolinite has shown dominant surface growth of nZVI particles ($>24.8 \pm 7.4$ nm) and positive zeta potential, suggesting domination of Fe⁰ nanoparticles (nZVI) characteristics. This surface-dependent variation led to higher and faster removal of oxy-anions with K-nZVI, i.e., chromium and arsenic (87.5 and 157.35 mg/g) than B-nZVI (18.4 and 86.9 mg/g). In comparison, B-nZVI has shown higher sorption of cations i.e., nickel and cadmium (36 mg/g and 46 mg/g) than K-nZVI (25 and 27 mg/g). XPS and pXRD analysis of reaction precipitates confirmed reductive sorption of chromium, co-precipitation/ complexation of arsenic, electrostatic attraction and complexation of nickel and cadmium as major removal mechanisms. Drastically higher total contaminant sorption capacities of B-nZVI (327 mg/g) and K-nZVI (372 mg/g) in multi-contaminant (Cr+As+Ni+Cd) solutions than individual capacities in mono-ionic solutions was due to co-operative effects and newer sites induced *via* sorption and redox-transformation of other ionic species. K-nZVI removed chromium and arsenic to below drinking water permissible limits whereas B-nZVI succeeded in separating nickel and cadmium to drinkable levels in groundwater, freshwater, river water, and wastewater samples, emphasizing their applicability in high cationic—low anionic and low cationic-higher anionic species contaminated waters, respectively.

Keywords: nZVI, sorption, kaolinite, bentonite, metals removal, reductive co-precipitation

1. Introduction

Water is a unique entity of the planet and one of the most critical resources required for balanced ecosystem functioning. According to recent estimates, three out of every ten people do not have access to contamination-free drinking water [1]. Tremendously increasing water use by nearly 1% per year has resulted in high water stress for over 2 billion people [2]. In an extensive range of contaminants, increasing concentrations of heavy metals and metalloids in water bodies represent an alarming environmental threat because of their non-degradability and environmental persistence [3]. Once introduced in the environment, these ions tend to bioaccumulate, impact the whole food chain and ultimately threaten human health [4, 5]. In a prevailing environmental condition, these ions can speciate in various ionic species [6]. For example- as shown in fig. S1 a-d, in circum-neutral pH conditions and oxidizing environment, arsenic (As) and chromium (Cr) speciate in anionic species, i.e., arsenate and chromate ions [7, 8], whereas nickel (Ni) and cadmium (Cd) stay in their cationic +2 form [9].

This variation in ionic behavior requires selectivity or a component additive approach as a critical component in the remediation technique [10]. Moreover, the co-contamination of ions with similar charge behavior can induce site competition in the system and may make the remediation even more challenging. Similarly, solutions contaminated with multiple ions of varying charge can also impact the treatment efficiency [11]. Several explored removal techniques include conventional methods that suffer from limited selectivity and sorption capacity, such as filtration, sedimentation, coagulation-flocculation, aerobic and anaerobic degradation, etc. [12]. Bioremediation, including phytoremediation, suffers from slower reaction kinetics [13]. Other remediation techniques are distillation, solvent extraction, microfiltration, ultra-filtration, reverse and forward osmosis, electrolysis, etc., with high power consumption and tedious setup and maintenance [14]. Sorption-assisted water treatment techniques involve cost-effectiveness, environmentally friendly nature, high selectivity,

removal capacity, process simplicity, no secondary contamination, and low power consumption, etc., and are therefore of prime interest to the scientific community [15]. Redox-sensitive nano-adsorbents, such as magnetic nanoparticles, Fe_3O_4 , graphene, etc., have recently emerged and explored for their added electron transferring ability at the surface-water interface [16, 17]. It can lead to simultaneous redox transformation of toxic metals, forming coprecipitate with insoluble metal oxy-hydroxides on the composite surface [18, 19].

Instant inert surface oxide shell formation and self-aggregation of these redox-sensitive nanoparticles in the natural environment generally limits their applicability [20]. Research showed that supporting surfaces, such as clays, graphene, biochar, charcoal, etc., can preserve their redox state [16, 21]. Clays dominate out of several supporting surfaces because of their natural abundance, eco-friendly nature, and high cation exchange capacity that can prevent secondary contamination [22]. Clays are hydrous alumino-silicates and have a flake-like structure. Based on the crystal structure, i.e., a combination of tetrahedral (T) and octahedral (O) layers, kaolinite (1:1- T:O type), and bentonite containing around 80% of montmorillonite (2:1- T-O-T type) are two major clays [23]. Both kaolinite and bentonite have been explored to support redox-sensitive nanoparticles like- nanoscale zerovalent iron (nZVI) [24, 25]. Despite a drastic variation in the crystal structure and material properties, i.e., kaolinite with non-swelling nature and less interlayer spacing leading to limited cation exchange capacity (CEC), while bentonite having swelling (>10 times) nature, and very high CEC, etc., surface-associated variations in growth behavior of redox-sensitive nanoparticles and its impact on contaminant sorption behavior are still unknown.

Recently researchers have synthesized different clay-nZVI composites for the removal of various contaminants. For example, Baldermann et al. supported NANO FER 25 nZVI suspension on bentonite clay and used it to remove trichloroethylene (TCE), where nanoparticles were attached only on the surface [26]. Shi et al. showed B-nZVI formed using

a liquid-phase reduction technique had around 18.7 mg/g of CrO_4^{2-} sorption capacity [27]. Whereas, Üzüm et al. found that kaolin-supported nZVI can remove Cu^{2+} and Co^{2+} ions with 140 mg/g and 25 mg/g of sorption capacity. Reductive co-precipitation of contaminants due to electron transfer from Fe^0 and its oxidation oxy-hydroxides [28]. So far, clays are only considered a supporting material to prevent Fe^0 nanoparticle agglomeration and preserve their reactivity [29].

However, dominating role of variation in crystal structure and properties of clays in deciding or controlling the sorption behavior of nZVI composites for various ionic contaminants is unknown. Here, based on the fundamental variations in crystal structures variation of different clays, we hypothesized that 1:1 clay having limited or no interlayer spacing and non-swelling nature could result in the growth of nZVI mostly on the surface. In contrast, swelling is widespread in 2:1 montmorillonite clay due to hydration [30]. It is reported that Na- bentonite can show two different swellings, i.e., crystalline swelling (limited d-spacing increase) and osmotic swelling resulting in a larger d-spacing increase (even $>50\text{Å}$) [31]. Osmotic swelling happens at a lower salt concentration ($<0.5\text{M}$) of monovalent ions [31]. Therefore, supporting nZVI on highly swelling 2:1 bentonite clay can lead to the growth of nanoparticles in inter-layer spaces. The variation in the growth behavior of Fe^0 nanoparticles on different clay surfaces can further alter the surface properties such as nanoparticles size, charge, and surface area, etc., leading to varying sorption behavior for ionic contaminants.

To test the hypothesis, B-nZVI and K-nZVI composites were synthesized and sorption behavior was tested in mono, co, and multi-contaminant systems by utilizing different contaminants, i.e., oxy-anions (chromium, arsenic), and metal cations (nickel, cadmium). Detailed batch sorption studies and surface characterization using dynamic light scattering (DLS), powder X-ray diffraction (pXRD), Fourier-transform infrared (FTIR) spectroscopy,

and X-ray photoelectron spectroscopy (XPS) were done to delineate preferential sorption of contaminants and associated removal mechanisms of the composites.

2. Materials and methods

2.1 Materials and chemicals

Clays used include- extra pure Na-bentonite (Loba Chemie Pvt. Ltd., India) with composition (wt%)- 54.9 % SiO₂, 19.2 % Al₂O₃, 8.3 % Fe₂O₃, 3.79 % Na₂O, 1.99 % MgO, 1 % K₂O and 0.17 % CaO [21], and kaolinite (Charco Chemicals, India) with composition- 55.51 % SiO₂, 28.6 % Al₂O₃, 0.6 % Fe₂O₃, 0.1 % Na₂O, 0.02 % MgO, 4.55 % K₂O and 0.06 % CaO. Chemicals purchased from Merck, Germany, are Ethanol, NaAsO₂ 0.05N solution, Ni(NO₃)₂·6H₂O, and FeCl₃·6H₂O. Merck, India supplied CdCl₂·H₂O, K₂Cr₂O₇, HNO₃, NaOH, NaBH₄, and NaNO₃. 18.2 MΩ.cm Milli-Q water was used for preparing all solutions.

2.2 Synthesis of nanocomposites

To synthesize bentonite and kaolinite supported nZVI (B-nZVI and K-nZVI, respectively), nanocomposites, clay, and iron salt with a 1:1 mass ratio were introduced to 4:1 ethanol: water mixture [16]. The suspension was sonicated for 30 minutes, followed by vigorous stirring. Then NaBH₄ (1M) was added dropwise at a flow rate of 4.5 mL/min to the suspension under constant stirring.

The reaction mixture was left for another 20 minutes on vigorous stirring after NaBH₄ addition to ensure complete reduction. Then the obtained precipitate was filtered, washed multiple times with ethanol and water, and vacuum dried.

2.3 Characterization of nanocomposites

Clay surface morphology was visualized using field emission scanning electron microscopy (FESEM, Carl Zeiss SUPRA- 55VP), and size distribution was obtained using particle size

analyzer (ZEN3600, Malvern, UK). Whereas synthesized nanocomposites were analyzed using FESEM and ultra-high-resolution transmission electron microscopy, i.e., UHR-FEG-TEM (JEOL, JEM 2100 F). Elemental composition, mapping, and line scans were obtained using EDAX analysis through INCA software (Oxford Instruments, X-Max) coupled with UHR-FEG-TEM. Specific surface area and pore size distribution using Micromeritics Gemini VII BET-N₂ surface area analyzer. The nitrogen adsorption/desorption isotherms are reported by BJH (Barret Joyner-Halenda) surface analysis method. Before analysis, samples were degassed in vacuum at 150 °C for 12 h. Crystallinity and phase characteristics were obtained by powder X-ray diffraction (pXRD) of materials. pXRD measurements were taken using benchtop powder X-ray diffractometer (Rigaku mini flex) having Cu K α = 1.54059 Å radiation at 40 kV/15 mA. Samples were scanned in the range of 5⁰-65⁰ 2 θ at 5⁰ per minute and step size of 0.02⁰. Surface functionality was interpreted using Fourier transform infrared spectroscopy (FTIR) by analyzing KBr pallets using Thermo-Scientific Nicolet iS5 coupled with the iD1 transmission accessory. Zeta Sizer (ZS-90, Malvern) coupled with MPT-2 pH auto-titrator was used to obtain zeta potential and point of zero charges (pH_{PZC}) of composites. Reaction precipitates were also analyzed using a PHI 5000 VersaProbe II (ULVAC-PHI Inc.) equipped with a monochromatic Al K α X-ray source (1486.7 eV) for XPS measurements. Elemental lines are charge referenced to C1s (C_xH_y) at 284.8 eV.

2.4 Batch sorption experiments and analytical techniques

At pH 6.5, 0.01 M NaNO₃ solutions were introduced with (i) mono contaminant system, i.e., arsenic, chromium, nickel, and cadmium individually, (ii) co-contaminant systems, i.e., anionic (An), i.e., arsenic-chromium and cationic (Ct), i.e., nickel-cadmium and (iii) multi-contaminant systems (MM), i.e., arsenic-chromium-nickel-cadmium. With a fixed weight of adsorbent, i.e., 20 mg, and a solution volume of 25 mL, sorption kinetics was performed at 20 mg/L concentrations of respective contaminants by varying the interaction time. At the same time,

sorption isotherm experiments were performed by varying contaminant concentrations in 10-60 mg/L range by keeping interaction time constant to 12 h, which is more than the obtained equilibrium time. Reaction mixtures were kept on shaking (200 RPM) at 25 °C. After the interaction, mixtures were centrifuged, and reaction precipitates were dried for further characterization. Whereas, supernatants were again filtered using 0.22 µm filter paper, acidified, and analyzed for respective contaminant concentrations using ICP-OES (Thermo iCAP-7400 series). Samples were also analyzed for released iron concentration after the interaction to ensure minimal secondary contamination. Sorption behavior was also evaluated (i) as a function of pH and (ii) in different types of water compositions, i.e., synthetic freshwater, groundwater, wastewater, and natural river water (compositions provided in table-S1a-b in supplementary information), to ensure environmental applicability of the composites. For that, 20 mg of adsorbent was taken in 25 mL of the solution with having 10 mg/L concentration of each metal ion. All the experiments were performed in duplicates, and errors are shown wherever significant (>5%) and required. Performed blanks include (i) all stated combinations of contaminated solutions without adding adsorbents and (ii) solutions containing composites without adding contaminants.

3. Results and discussion

3.1 Surface characteristics and particles growth behavior

Morphology, composition, and growth mechanisms

The sheet-like structure of both bentonite and kaolinite can be visualized through SEM images in fig. S2a, and S3a. FESEM images showed that most of the clay flakes were of size <2µm while obtained hydrodynamic diameter using particle size analyzer (Fig. S2b, and S3b), showed a size distribution upto 100µm with most particles <10µm. This increased size corresponds to aggregates formed in suspension. After nZVI growth, clay surfaces show the presence of spherical nanoparticles, as observed in HRTEM images in fig. 1 a-c. FESEM

images of B-nZVI (Fig. S2 c-d) showed a clear variation having bright interlayer cross-sections compared to K-nZVI where Fe⁰ nanospheres were clearly visible only attached on the surface (Fig. S3 c-d).

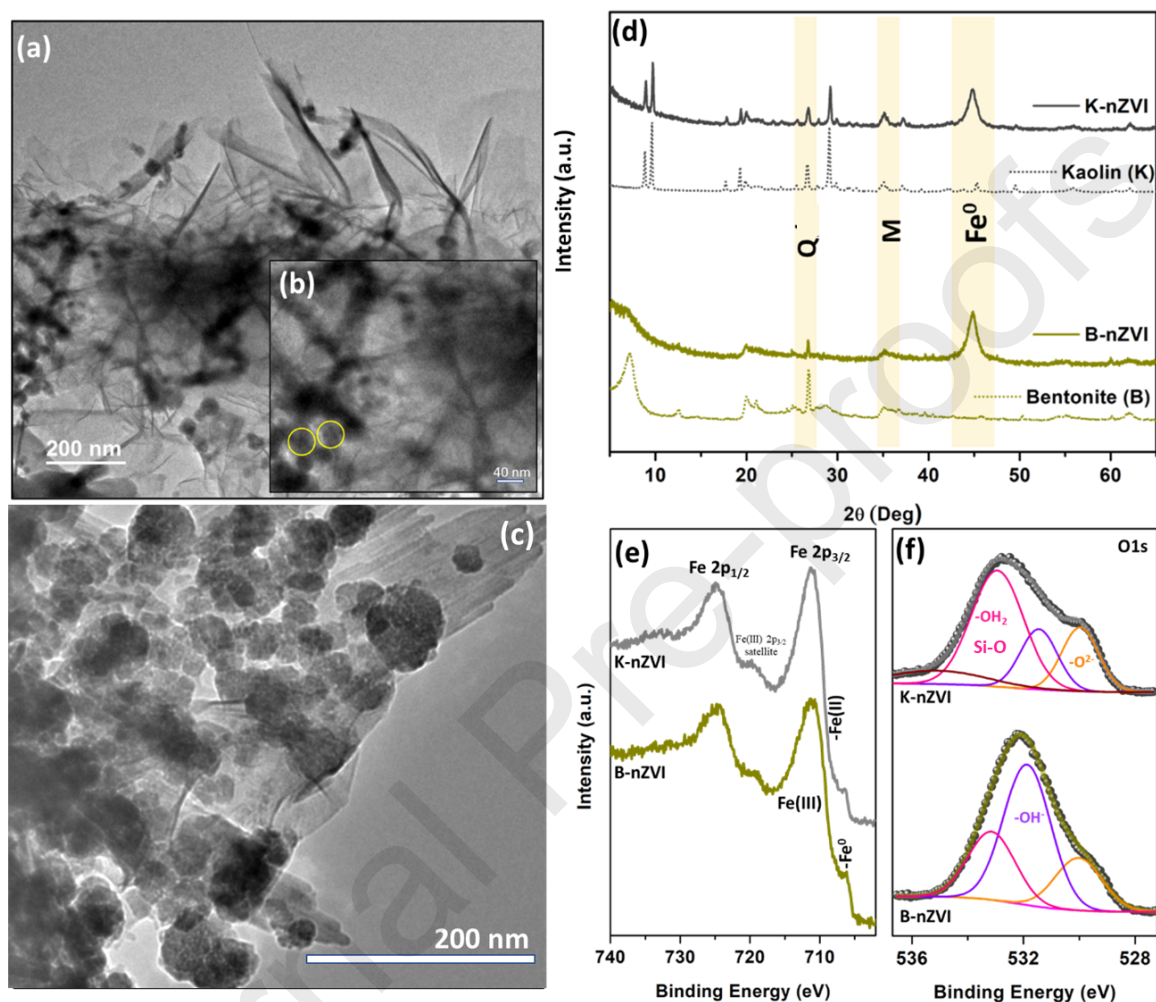
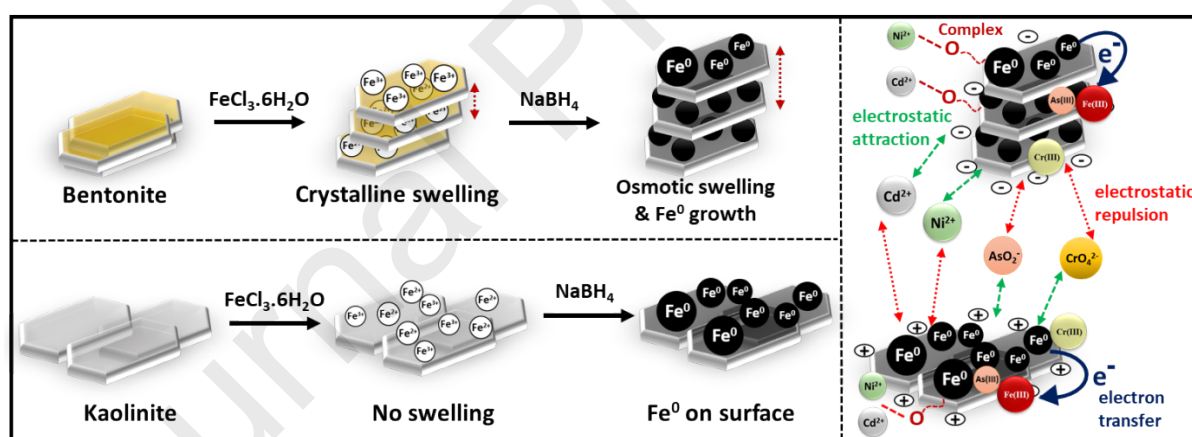


Fig.1 TEM images of (a) and inset (b) B-nZVI, (c) K-nZVI, (d) pXRD spectra of clay and nZVI composites [Q= quartz, M= magnetite] and XPS spectra of B-nZVI and K-nZVI for (e) Fe2p and (f) O1s regions

Particles size distribution analysis using multiple TEM images (Fig. 1 a-c, Fig. S2 e-f, and Fig. S3 e-f) showed two distinct size distributions of Fe⁰ nanoparticles in B-nZVI, i.e., 5.83 ± 2.6 nm and 20.65 ± 8.7 nm corresponding to growth of particles in the interlayers and surface of bentonite, respectively. In contrast, iron nanoparticles covered the surface of kaolinite with a diameter of 24.8 ± 7.4 nm. Elemental mapping in fig. S4 a, b showed the enhanced intensity of

iron signal over spherical particles and the presence of oxygen and silicon in the background supporting the growth of iron nanoparticles on clay surfaces. Fig. 1d shows the pXRD pattern of clays and synthesized nanocomposites. The characteristic d-001 peak of bentonite around $2\theta = 7.14^\circ$ corresponding to an interlayer spacing of 1.27 nm [32] shifted and broadened after iron loading, suggesting the broadening of interlayer space which can be attributed to Fe^0 nucleation and growth in interlayers. Earlier, Son et al. have also observed a peak shift of d001 in bentonite after iron-oxide loading due to formation of polycations and particles in the interlayers [33]. In K-nZVI, the d-001 peak of kaolinite around $2\theta = 12^\circ$ was present with no shifting or broadening, supporting no significant change in the interlayer spacing [34]. Simultaneously, the generation of characteristic Fe^0 peak near 44.8° , along with the absence of iron oxide peaks [35, 36], suggests that iron particles were in preserved redox state on both clay surfaces with no dominant crystalline iron-oxide phases or thick oxide shells.



Scheme 1 Synthesis and growth mechanisms of nZVI on bentonite and kaolinite surfaces and respective contaminant removal mechanisms.

The surface of composites was further evaluated using XPS spectra and by fitting Fe2p and O1s regions (fig. 1 e-f). Obtained peaks around 706.9 eV, 711.1 eV, 724.9 eV, and 719.9 eV of binding energies corresponded to Fe(0) 2p_{3/2}, Fe(III) 2p_{3/2}, Fe(III) 2p_{1/2} and satellite peak of Fe(III) 2p_{3/2}. Fitting reveals the presence of Fe(II) and Fe(III) along with Fe^0 on the surface in

both kaolinite and bentonite [37]. It can be attributed to a very thin shell of iron-oxy—hydroxides on the surface of elemental iron nanoparticles. Higher Fe⁰ content on bentonite surface compared to kaolinite can be attributed to nanoparticles coverage with bentonite flakes as observed in TEM images.

In summary, two distinct size fractions of nZVI in bentonite, broadening of interlayer spacing as obtained from pXRD, and higher Fe⁰ content in B-nZVI compared to no change in d001 peak of kaolinite after nZVI growth, and >20nm particles attached on the surface, suggest the following , iron nanoparticles growth mechanisms (Scheme 1): initially, the addition of bentonite in an interfacial solution can result in its crystalline swelling, which allows iron ions to enter and adsorb in the inter-layer spaces and on the surface as well. Once the addition of NaBH₄ begins, iron particles start to nucleate, and simultaneously interlayer spacing of bentonite clay increases due to its osmotic swelling [38, 39]. It may easily allow iron nanoparticles to grow in the interlayer spaces and on the surface. On the other hand, kaolinite is 1:1 clay and does not swell, which results in the surface sorption and growth of iron nanoparticles [25].

Surface area and pore distribution

BET-N₂ adsorption-desorption isotherms are shown in fig.S5 a, c. Pertaining to limited inter-layer space, kaolinite clay showed a BET-N₂ surface area of 3.15 m²/g, whereas it was 24.5 m²/g for bentonite [40, 41]. Literature reports show that bare nZVI particles have a surface area of around 20-25 m²/g [42, 43]. After nZVI growth, bentonite surface area increased further to 31.1 m²/g, corresponding to the growth of very small (5-7 nm) iron nanoparticles. . In contrast, K-nZVI showed a surface area of 19.4 m²/g which was higher than kaolinite but was in range with the surface area of bare nZVI particles [44, 45]. A decrease in the pores (\approx 4 nm) having a maximum volume in B-nZVI compared to bentonite suggests nZVI growth in available pores

(fig. S5b). While an increase in the pore volume (fig. S5d) in K-nZVI can be attributed to nanoscale particles growth on the surface. These observations further support the proposed Fe^0 particles growth mechanisms on different clay surfaces. Further details of obtained surface area, average pore diameter, and cumulative pore volume are provided in table S2. B-nZVI has shown a slightly higher cumulative pore volume than bentonite, which may be due to the growth of some nZVI particles on the clay surface.

Surface functionality and charge

Both kaolinite and bentonite shared almost similar surface functionality. FT-IR spectra (fig. S5e) showed a broad peak around 3430 cm^{-1} for -OH group stretching. 1044 cm^{-1} peak was due to Si-O bending vibration, while antisymmetric Si-O-Si stretching vibration caused an adsorption peak near 797 cm^{-1} [46]. Kaolinite group minerals show -OH bands at 3696 , 3669 and 3651 cm^{-1} beside the 3619 cm^{-1} inner hydroxyl group band while 1632 cm^{-1} peak of O-H reflected crystal water in clays lattice [47]. A shift in the 1632 cm^{-1} O-H peak and the generation of an adsorption band at 670 cm^{-1} was due to the symmetric Fe-O stretch of goethite ($\alpha\text{-FeOOH}$)[48].

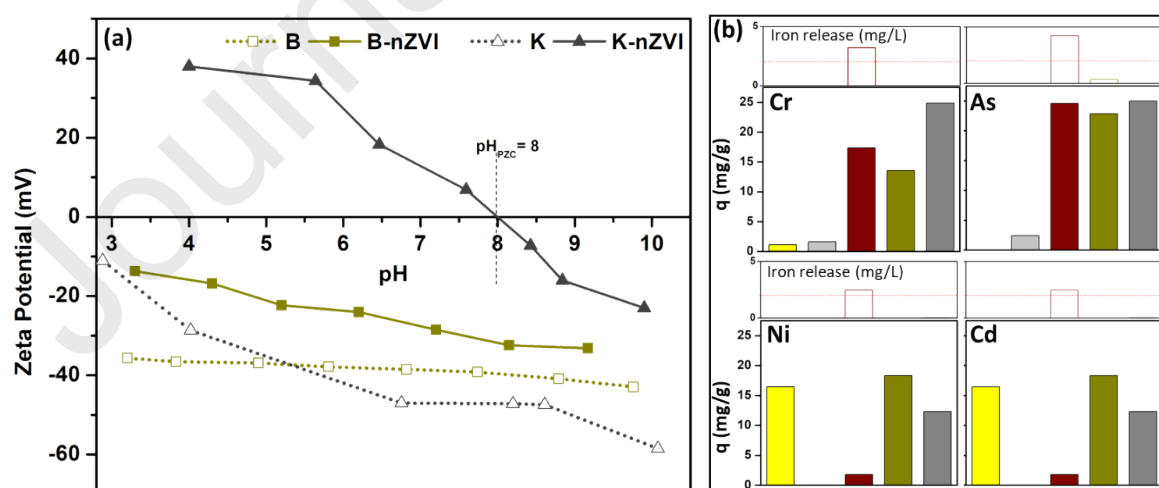


Fig.2 (a) Zeta potential at varying pH for clays and synthesized nanocomposites and (b) Sorption capacity of raw constituents of nanocomposites i.e., Bentonite, Kaolinite and nZVI

and synthesized composites i.e., B-nZVI and K-nZVI [m= 20 mg, V= 20 mL, C₀= 20 mg/L, T= 25°C, RPM= 200, pH= 6.5, t= 12h]

This variation in the growth behavior of nZVI particles, i.e., the domination of bentonite in B-nZVI and of nZVI in K-nZVI, can also be correlated with variation in the zeta potentials of various composites (fig. 2a). The negative zeta potential of both the clays, i.e., <-30 mV, can be attributed to isomorphous substitution in their crystal structures [49]. It decreased but remained negative even after nZVI growth in the case of B-nZVI, confirming bentonite domination. Whereas, after nZVI growth, K-nZVI shows the point of zero-charge at pH=8 i.e., at pH<8 K-nZVI has positive zeta potential. The positive zeta potential can be attributed to partial oxidation of nZVI particles and protonation of surface oxide layer. Therefore, in the environmentally relevant pH conditions (pH= 6-8) B-nZVI holds a negative charge, whereas K-nZVI was dominantly positive. This variation resulted from the drastic difference in nZVI growth behavior on both surfaces and is crucial for the adsorbent's selectivity towards specific toxic ions, as observed in later sections.

3.2 Contaminant sorption behavior and mechanisms

Preliminary sorption experiments with raw constituents of the composites i.e., bentonite and kaolinite clays and bare nZVI particles, were performed for all the studied contaminants and compared for respective sorption capacities with the synthesized nanocomposites. Results in fig. 2b show minimal sorption of oxy-anions (<2.5 mg/g) with both clays. Bare nZVI show significant sorption of oxy-anions but limited sorption of cationic species (< 5.5 mg/g). In comparison, synthesized nanocomposites showed higher removal of both cations (>18 mg/g) and oxy-anions (>13.5 mg/g). In all the cases, iron release from bare nZVI particles was higher than the WHO-defined permissible limit of 2 mg/L for drinking water. Whereas no significant iron release was observed in the case of nanocomposites. Results confirm that nanocomposites

advance their raw constituents regarding contaminant sorption capacities and prevent the secondary release of pollutants. Interestingly, both B-nZVI and K-nZVI showed a drastic variation in contaminant-specific sorption capacities. At a fixed concentration of toxic anions and cations, B-nZVI showed comparatively higher removal of nickel and cadmium, whereas K-nZVI separated chromium and arsenic with high efficiency (fig. 2b). This variation in sorption capacities might be directly correlated with the positive and negative zeta potentials of K-nZVI and B-nZVI (fig. 2a), respectively, allowing faster interaction and bulk transfer of oppositely charged ions on the surface.

After the sorption of toxic ions, reaction precipitates were collected and thoroughly characterized for change in surface charge, crystallinity, functionality, and redox composition to delineate various involved removal mechanisms. Interaction and removal mechanisms were found to be varying for different contaminants for B-nZVI and K-nZVI and are described below in detail.

Chromium

Chromium which speciate in the form of CrO_4^{2-} oxy-anions, had varying interaction with B-nZVI and K-nZVI. Zeta potential (fig. 3 a-b) of B-nZVI in 0.01M NaNO_3 solution was -16.7 ± 1.3 mV which decreased to -13.3 ± 0.4 mV after interaction with chromate ions. The sole involvement of electrostatic attraction should have resulted in either increased negative zeta potential or electrostatic repulsion with chromate ions, suggesting the involvement of other removal mechanisms. Similarly, zeta potential of K-nZVI was $+12.1 \pm 0.7$ mV which decreased to $+8.5 \pm 1.3$ mV after interaction with chromate ions supporting the involvement of electrostatic attraction. But, a slight decrease in zeta potential points out the presence of different species of chromium on K-nZVI surface as well. These observations were further supported by pXRD spectra (fig. 3c-d), which showed a slight decrease in the intensity of Fe^0 peak in B-nZVI and

little oxidation of iron on B-nZVI surface, suggesting limited electron transfer and redox-transformation in the system leading to limited interaction of B—nZVI with chromium. K-nZVI showed a drastic decrease in 44.8° Fe^0 peak and generation of 30° and 35° intense iron-oxide peaks suggesting intense electron transfer and iron oxidation. FTIR spectra (fig. 3 e-f) also showed the enhanced intensity of 530 cm^{-1} Fe-O stretching. Redox transformation of chromium and composites was further confirmed by obtaining XPS survey scans (fig. S6a-b). High-resolution scans for Fe2p (fig. S6c—d), O1s (Fig. 4a) and Cr2p regions (fig. 4f). Fe^0 associated peak near 707 eV disappeared after interaction with chromium in both B—nZVI and K-nZVI confirming electron transfer and consumption of Fe^0 . In correspondence, Fe(II) and Fe(III) contribution increased on the surface.

Cr2P spectra showed a dominant presence (72.8% and 79.6%) of Cr(III) near 577 eV on B-nZVI and K-nZVI surfaces, confirming the reduction of chromium on both surfaces [50, 51]. K-nZVI showed higher intensity of Cr2p-associated peaks compared to B-nZVI. O1s spectra showed the dominance of $-\text{OH}^-$ functional groups in B-nZVI and both $-\text{OH}^-$ and $-\text{O}^{2-}$ groups in K-nZVI (fig. 4a) after interaction with chromium, suggesting the simultaneous formation of iron oxides/oxy-hydroxides and chromium oxide/oxy-hydroxide. In combination, zeta potential, pXRD, and XPS data confirm strong interaction and higher redox-transformation of chromate ions with K-nZVI and co-precipitation with formed iron-oxy-hydroxides compared to B-nZVI, which was also supported by experimental sorption capacities data provided in later sections. Results indicate that in the case of B-nZVI, slower CrO_4^{2-} sorption corresponds to initial electrostatic repulsion followed by electron release from Fe^0 and chromate ions reduction and sorption or co-precipitation of Cr(III) on B-nZVI surface. In contrast, K-nZVI showed strong electrostatic attraction of chromate ions on K-nZVI surface, followed by its reduction on the surface via electron transfer from Fe^0 core and attachment of Cr(III) with FeOOH . In

multi-metallic solutions, both K-nZVI and B-nZVI showed a decrease in Cr2p peaks intensity with a decrease in Cr(III) abundance to 71% and 68%, respectively (Fig. 4f).

Arsenic

After the sorption of arsenic, both B-nZVI and K-nZVI showed a drastic decrease of zeta potential from -16.7 ± 1.3 mV and $+12.1 \pm 0.7$ mV to -33.9 ± 1.1 mV and -17.9 ± 2.4 mV, respectively (fig. 3a-b). pXRD spectra (fig. 3c-d) showed a decrease in 44.8° Fe⁰ peak with a slight increase in 35° iron oxide peak and 46° FeOOH peak in B-nZVI whereas K-nZVI showed the generation of strong 30° and broad 35° iron oxide peaks. FTIR spectra showed the generation of 805cm^{-1} stretching due to FeOOH in B-nZVI along with 530cm^{-1} and 580cm^{-1} Fe-O stretching (fig. 8e—f).

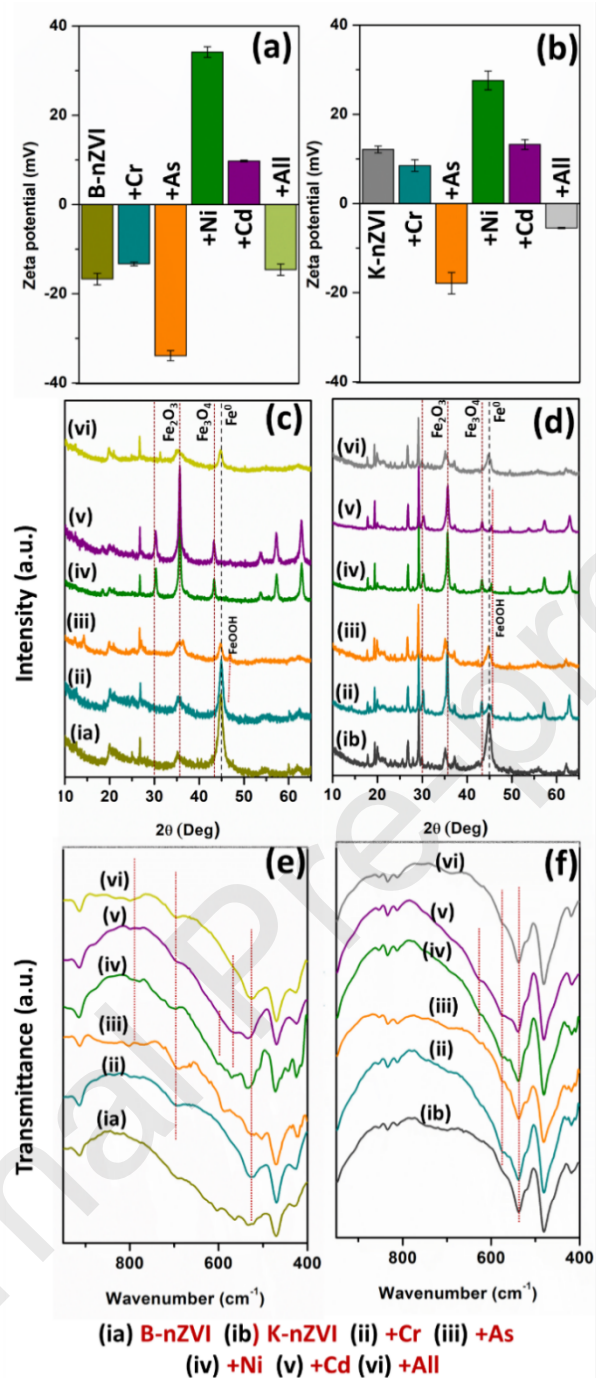


Fig. 3 (a, b) zeta potential, (c, d) pXRD and (e—f) FTIR spectra obtained for different reaction precipitates after sorption experiments using B-nZVI and K-nZVI respectively [(ia) B-nZVI, (ib) K—nZVI, (ii) Cr, (iii) As, (iv) Ni, (v) Cd, and (vi) Cr-As-Ni-Cd].

XPS spectra (fig. 4g) of As3d region showed the presence of As(III) on both B—nZVI and K-nZVI surfaces. The As3d spectrum consists of the As 3d_{5/2} and As 3d_{3/2} lines, separated by 0.69

eV, area ratio 3:2, assigned to As(III)-O(H) bonding. Redox transformation of As(III) is hard to predict in the multi-metallic system due to the presence of Cr3p signals. However, results suggest dominant As(III) complexation with iron oxy-hydroxide..

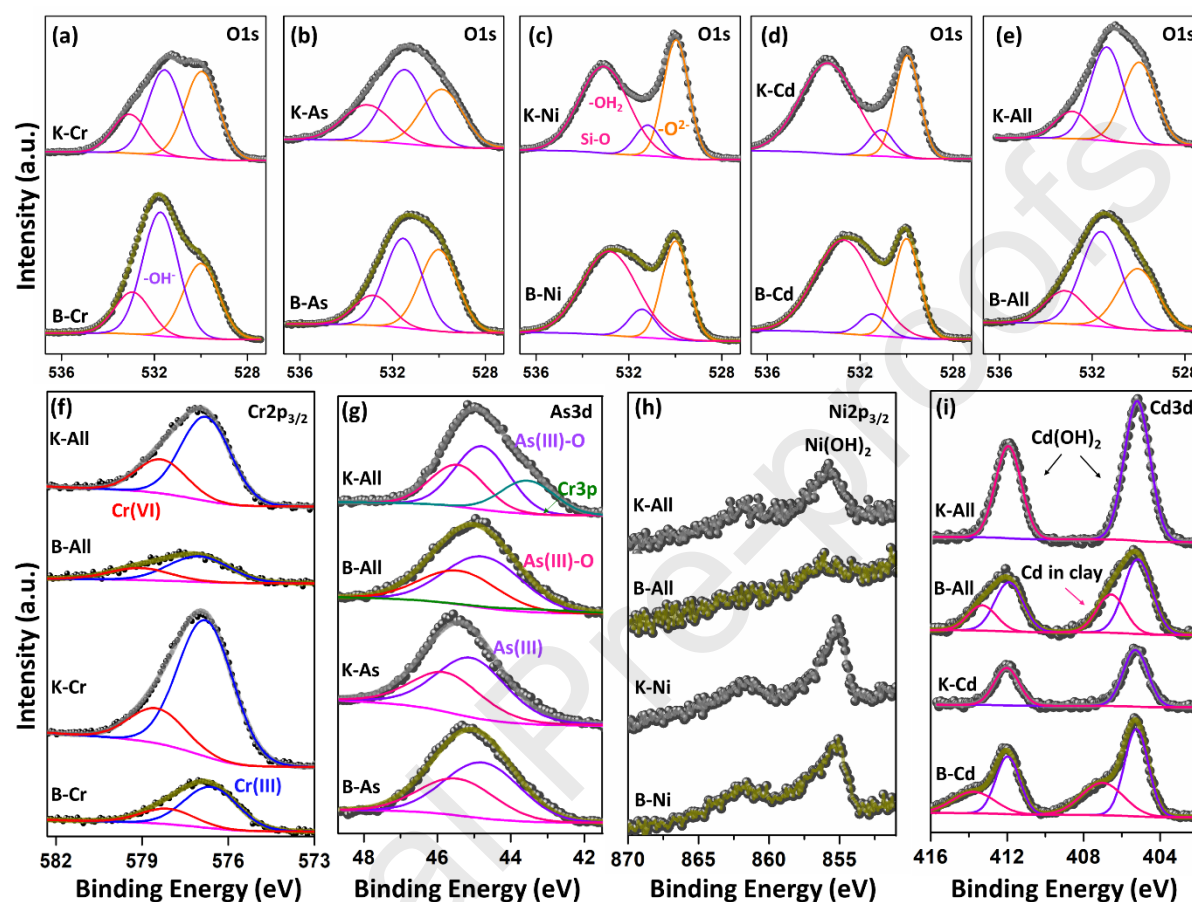


Fig. 4 XPS data for different composites and reaction precipitates showing fitted (a-e) O1s spectra for reaction residues before and after sorption experiments for B-nZVI and K-nZVI, respectively, and spectral fits for (f) Cr $2p_{3/2}$, (g) As $3d$, (h) Ni $2p_{3/2}$, and (i) Cd $3d$ regions.

The XPS data indicate that arsenic is trivalent as added to solution present in the form of As(OH) $_3$ (aq) or HAsO $_2$ (aq) specie. Arsenic can get oxidized to As(V) in a surface water environment where Eh is higher. The presence of nZVI may lower Eh, and arsenic can be reduced to As(III) at contact with nZVI. Presence of arsenic dominantly in the form of As(OH) $_3$ leads to ligand exchange, and switching from Fe-OH $_2^+$ to Fe-O-As(OH) $_2$ might explain the decrease in zeta potential.

Nickel

Both B-nZVI and K-nZVI showed a change in zeta potential to higher positive value. A drastic increase in zeta potential from -16.7 ± 1.3 mV to $+34.2 \pm 1.2$ mV in B-nZVI justifies high electrostatic attraction of Ni^{2+} (fig. 3a-b). Further, pXRD spectra (fig. 3c-d) showed the generation of 30° and 35° , and 43° intense iron oxide peaks and complete disappearance of Fe^0 peak in B-nZVI and presence with very low intensity in K-nZVI. Observation suggests formation of a very thick iron oxide shell on Fe^0 core. FTIR spectra (fig. 4e-f) further supported this observation and showed generation of 530 cm^{-1} , 570 cm^{-1} , and 630 cm^{-1} Fe—O stretching along with 705 cm^{-1} and 805 cm^{-1} bands due to FeOOH . Standard redox potential of $\text{Ni}^{2+}/\text{Ni}^0$ is -0.26 V at 298 K and is well above $\text{Fe}^{2+}/\text{Fe}^0$ (-0.44 V, 298 K) potential which suggest probable reduction of Ni^{2+} in Ni^0 [52]. But, Ni2p XPS spectra (fig. 4h) showed presence of Ni(II) peak in the region of 854.9 eV corresponding to $\text{Ni}(\text{OH})_2$ suggesting complexation and co-precipitation of nickel.

Cadmium

Similar to nickel, Cd^{2+} sorption also resulted in an increase in zeta potential from -16.7 ± 1.3 mV to $+9.7 \pm 0.2$ mV in B-nZVI suggested strong electrostatic attraction (fig. 3a). Whereas, only a slight increase in zeta potential value from $+12.1 \pm 0.7$ mV to $+13.1 \pm 1.1$ mV was observed in K-nZVI (fig. 3b). pXRD and FTIR observations were also similar to nickel, where intense iron-oxide shell generation was observed in the system. Cd3d XPS spectra (fig. 4i) showed the presence of Cd(II) in the system. Standard redox potential of $\text{Cd}^{2+}/\text{Cd}^0$ is -0.40 V at 298 K and is very near to $\text{Fe}^{2+}/\text{Fe}^0$ (-0.44 V, 298 K) potential suggesting no reduction of cadmium and probable removal via electrostatic attraction, complexation, and co-precipitation of cadmium.

In summary, dominant removal mechanisms were reductive co-precipitation of chromium, complexation of arsenic, electrostatic attraction and co-precipitation of nickel and cadmium with generated iron-oxy-hydroxide shell.

3.3 Sorption behavior in different contaminant systems: removal kinetics

Mono-ionic contaminant exposure

Aqueous solutions contaminated with single ionic species were reacted with both B-nZVI and K-nZVI to test the comparative preference of the composites. Results in fig. 5 a-d show that sorption equilibrium was achieved within 3h of interaction time for all contaminants.

K-nZVI achieved sorption equilibrium faster for chromium (~1h) and arsenic (~10min) compared to B-nZVI (~6h and 1h, respectively). In addition, 75% removal of chromium was achieved within 2 min of interaction with K-nZVI, whereas it was only 24% for B-nZVI. Arsenic removal was 78% within 2 min of interaction with K-nZVI compared to 52% for B-nZVI. After equilibration, near complete removal of chromium and arsenic was observed with K-nZVI but not with B-nZVI. Oppositely, B-nZVI showed faster removal of cadmium (56%) and nickel (45%) within 2 min of interaction compared to K-nZVI (27% of nickel and 33% of cadmium). These observations conclude preferential and quasi-instantaneous removal of anionic species with positively charged K-nZVI and cationic species with negatively charged B-nZVI due to both favored chemical binding and electrostatic attractions.

Insights on adsorption kinetics were modeling obtained through kinetic modeling of experimental data using pseudo-second order and general order models. The first one presumes the order of a reaction to be 2 whereas the latter suggests that the order of a reaction shouldn't be presumed but calculated using experimental data [53].

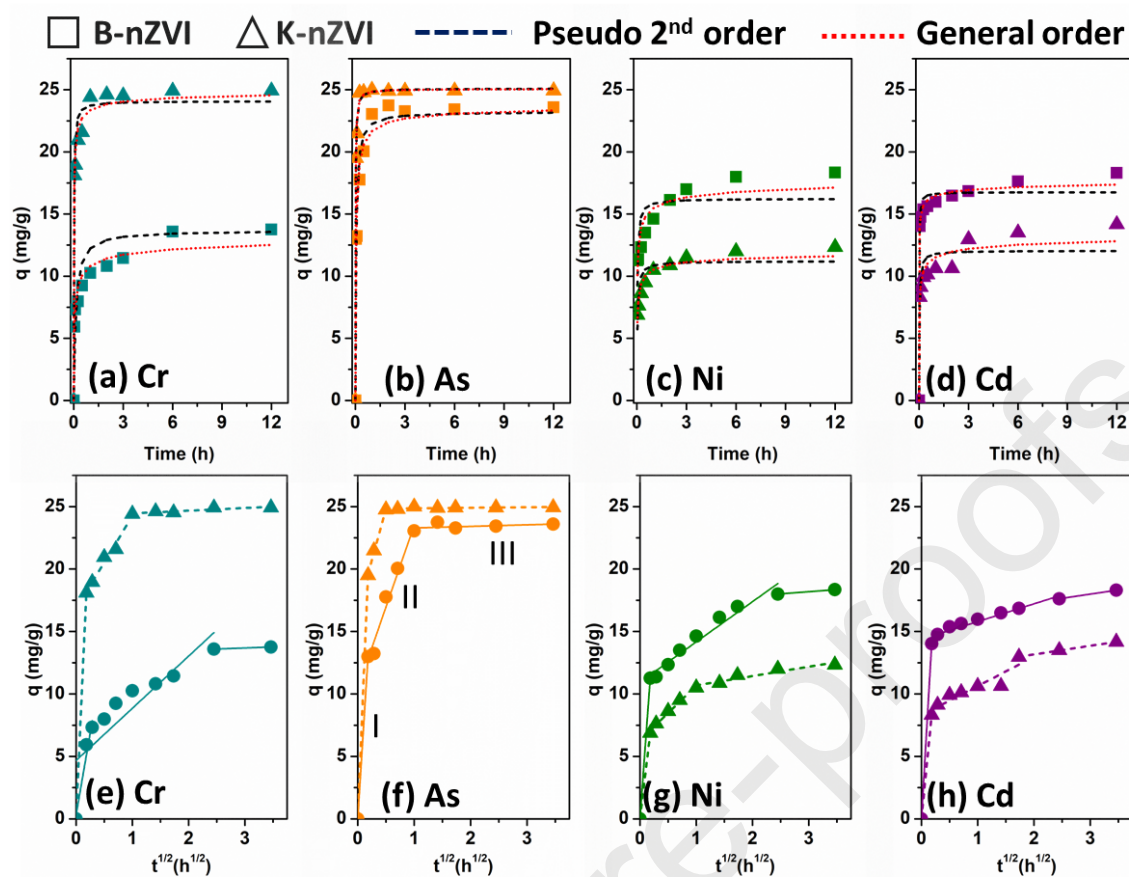


Fig.5 (a-d) effect of interaction time, reaction kinetics modeling and (e-h) intra-particle diffusion (IPD) modeling of B-nZVI and K-nZVI for mono-ionic contaminant system [$C_0=20$ mg/L, $V=25$ mL, $m=20$ mg, 200 RPM and 25°C .]

Therefore, the general order model provides information about equilibrium sorption capacity, rate constant, and reaction order and is a three-parameter model[54]. Models fit in fig. 5 a-d and obtained parameters in table S3 show that the general order model fits well compared to pseudo-second order for all contaminants and therefore justifies varying reaction orders for different contaminants. The reaction order ranged from 2 to 5, suggesting that both composites follow higher order kinetics for contaminants removal. Intra-particle diffusion (IPD) model in fig. 5 e-h show three different linear segments corresponding to (i) initial bulk transfer to the adsorbent surface, (ii) diffusion of adsorbate in the meso, macro, and micropores, and (iii) final equilibrium stage and, in mono-ionic contaminant systems, the same trend was observed in

most of the cases. Here the three segments can be tentatively attributed to faster adsorption followed by redox transformation (for chromium and arsenic) and/or co-precipitation and final equilibrium stage [55]. Intercept values for IPD were in order $Cr < As < Ni < Cd$ for B-nZVI while it was $As < Cr < Cd < Ni$ for K-nZVI suggesting limited bulk transport and comparatively longer IPD stage for chromium and arsenic with B-nZVI than K-nZVI suggesting slower redox transformation and co-precipitation on B-nZVI surface. Whereas, Ni^{2+} and Cd^{2+} exhibited limited bulk transfer and shorter IPD stage on K-nZVI surface compared to B-nZVI, suggesting limited metal cations removal capacity of K-nZVI than B-nZVI.

Co-ionic contaminant exposure

Remediation of water bodies contaminated with multiple similar charged toxicant ions can be of higher environmental relevance compared to mono-ionic contamination. The presence of multiple contaminants can either induce competitive sorption or co-operative sorption and, therefore can impact the total metal sorption capacity of the composites.

To understand the behavior of B-nZVI and K-nZVI in co-ionic systems, composites were reacted with aqueous solutions contaminated with Cr-As and Ni-Cd to represent anionic (An) and cationic (Ct) systems, respectively. Similar to mono-ionic system, K-nZVI showed faster and higher removal of both chromium and arsenic (fig. S7 a-b). Parameters obtained from well fitted general order model provide reaction order in the range of 3-5 (table S3b). IPD modeling in fig. 6 a-d also show higher bulk transport of chromium and arsenic to the K-nZVI surface compared to B-nZVI. Equilibrium was not achieved completely in case of B-nZVI for both chromium and arsenic suggesting removal at a slower rate. In comparison to mono-ionic system, removal of Ni^{2+} and Cd^{2+} decreased slightly for B-nZVI in co-contaminant system (fig. S7 c-d). Corresponding to near equal bulk transfer and similar IPD curve slope, both K-nZVI and B-nZVI showed removal of Ni^{2+} and Cd^{2+} at a near equal rate (fig. 6 c-d). These

observations further suggest a simultaneous increase in the cations removal capacity for K-nZVI in co-ionic system containing nickel and cadmium.

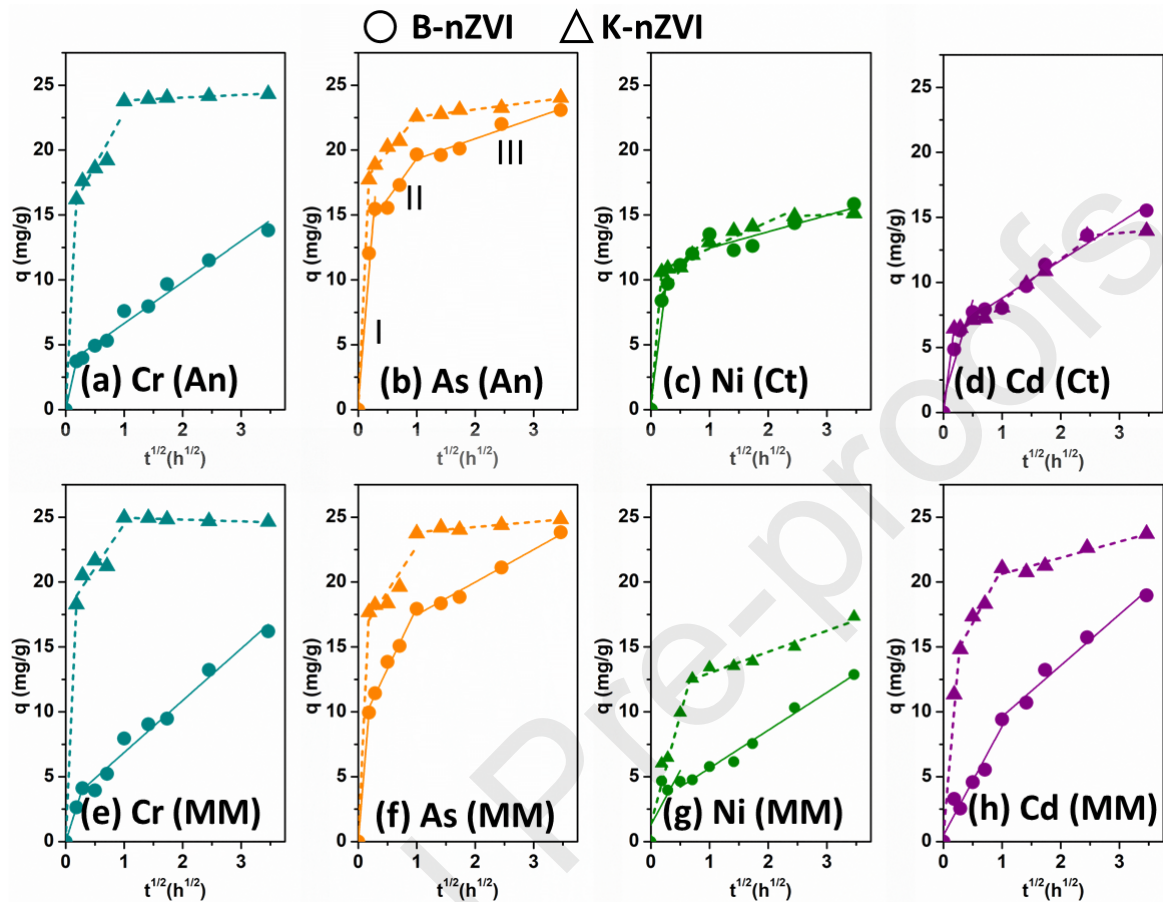


Fig. 6 Intra particle diffusion modeling for B-nZVI and K-nZVI in (a-d) co-ionic and (e-h) multi-ionic contaminant systems [$m=20$ mg, $V=20$ mL, $C_0=20$ mg/L each, $T=25^\circ\text{C}$, RPM=200, pH= 6.5, $t=0-12$ h]

Multi-ionic contaminant exposure

Water streams can receive toxic ions through several anthropogenic activities including wastes from different industrial outlets that can contaminate river and groundwater bodies with multiple ionic species. Therefore, it is essential to test the efficiency and behavior of synthesized composites in multi—ionic contaminant solutions. Here, multi-contaminant solutions constitute of equal concentrations of chromium, arsenic, nickel, and cadmium.

The simultaneous presence of both cationic and anionic contaminant species led to drastic variations in the sorption behavior of B-nZVI and K-nZVI compared to mono-ionic solutions (fig. S7 e-h). Enhanced sorption of oxy-anions was observed but with the limited bulk transfer of adsorbate and longer and slower IPD stage in B-nZVI. In addition, no sorption equilibrium was achieved in B-nZVI in the studied time frame of 12h (fig. S7 e-h). IPD model (fig. 6 e-h) showed the change in intercept values of B-nZVI and K-nZVI from 3.4 mg/g and 14.6 mg/g to 4.6 mg/g and 16.8 mg/g for chromium in multi-contaminant system, suggesting enhanced bulk transport of chromium on both B-nZVI and K-nZVI surfaces. Whereas arsenic showed a slight decrease in IPD intercept i.e., from 10.4 mg/g and 16.6 mg/g to 8.6 mg/g and 15.8 mg/g. At the same time, B-nZVI showed a drastic decrease in bulk transport of Ni^{2+} (from 10.9 mg/g to 2.7 mg/g) and Cd^{2+} (14.4 mg/g to 5.7 mg/g), suggesting initial sorption sites competition between nickel and cadmium on B-nZVI surface [56]. K-nZVI showed enhanced intercept values from 6.3 mg/g to 11.3 mg/g for Ni^{2+} and 8.3 mg/g to 12.6 mg/g for Cd^{2+} suggesting co-operative effects. The mechanism can further be supported using observations from mono-ionic solutions, which showed faster sorption of oxy-anions on K-nZVI that caused B-nZVI zeta potential to decrease from $+12.1 \pm 0.7$ mV to $+8.5 \pm 1.3$ mV for chromium and -33.9 ± 1.1 mV for arsenic. Similarly, in multi-ionic contaminated solutions, initial faster attraction of oxy-anions to K-nZVI surface turned the surface charge to negative and creates an electrostatically favorable environment for heavy metal cations. In stage-2, electron transfer from nZVI led to redox-transformation of chromium, and strong complexation of arsenic and co-precipitation of nickel and cadmium as confirmed using XPS and FTIR analysis. Fitting of experimental data in non-linear kinetic models also showed comparatively best fit with general order where the order of reaction was found in range of 2-6 (table S3c).

3.4 Impact of varying contaminant concentrations

Mono-contaminant aqueous solutions of varying concentrations of respective contaminant were reacted with the composites to understand the impact of increasing contaminant concentration on the sorption capacities of B-nZVI and K-nZVI. Results in fig. 7 a-d show an increase in the sorption capacity of the composites with increasing contaminant's concentration followed by plateau formation with the saturation of sorption sites. K-nZVI showed continuous increase in sorption capacities for chromium and arsenic oxy-anions when B-nZVI formed a plateau for chromium and showed a comparatively slower increase in arsenic sorption capacity. In contrast, K-nZVI showed site saturation and formation of plateau for Ni^{2+} and Cd^{2+} whereas higher removal capacity and continuous increase in sorption capacity of B-nZVI was observed for cationic species.

To obtain the information about maximum sorption capacities, nature of adsorbent surface, and removal mechanisms, non-linear sorption isotherm modeling using Langmuir, Freundlich, and Sips models was performed. In general, Langmuir isotherm assumes monolayer sorption with homogeneous nature of adsorbent surface, whereas Freundlich assumes a heterogeneous surface and multi-layer stacking of adsorbate molecules [57]. Both of these isotherms are two-parameter models whereas Sips isotherm which is a combination of Freundlich (at low concentrations) and Langmuir (at higher concentrations) isotherms, is a three-parameter model [58]. Further description of sorption isotherm models is provided in the section 3 of supplementary information. Results in fig.7 a-d and parameters in table S4a show that Sips isotherm best fits all the contaminants, confirming the heterogeneous nature of both composites. In all cases, $n \neq 1$ further confirmed the heterogeneous nature of composites surface. Obtained maximum sorption capacities of B-nZVI for chromium and arsenic were 18.4 mg/g and 86.8 mg/g which were comparatively lesser than K-nZVI i.e., 87.4 mg/g for chromium and 157.3 mg/g for arsenic. In contrast, B-nZVI showed higher sorption capacities for Ni^{2+} (36 mg/g) and Cd^{2+} (46 mg/g) compared to K-nZVI (25 mg/g and 27 mg/g,

respectively). These experimental observations further confirm preferential sorption of cationic species on B-nZVI and anionic species on K-nZVI surface.

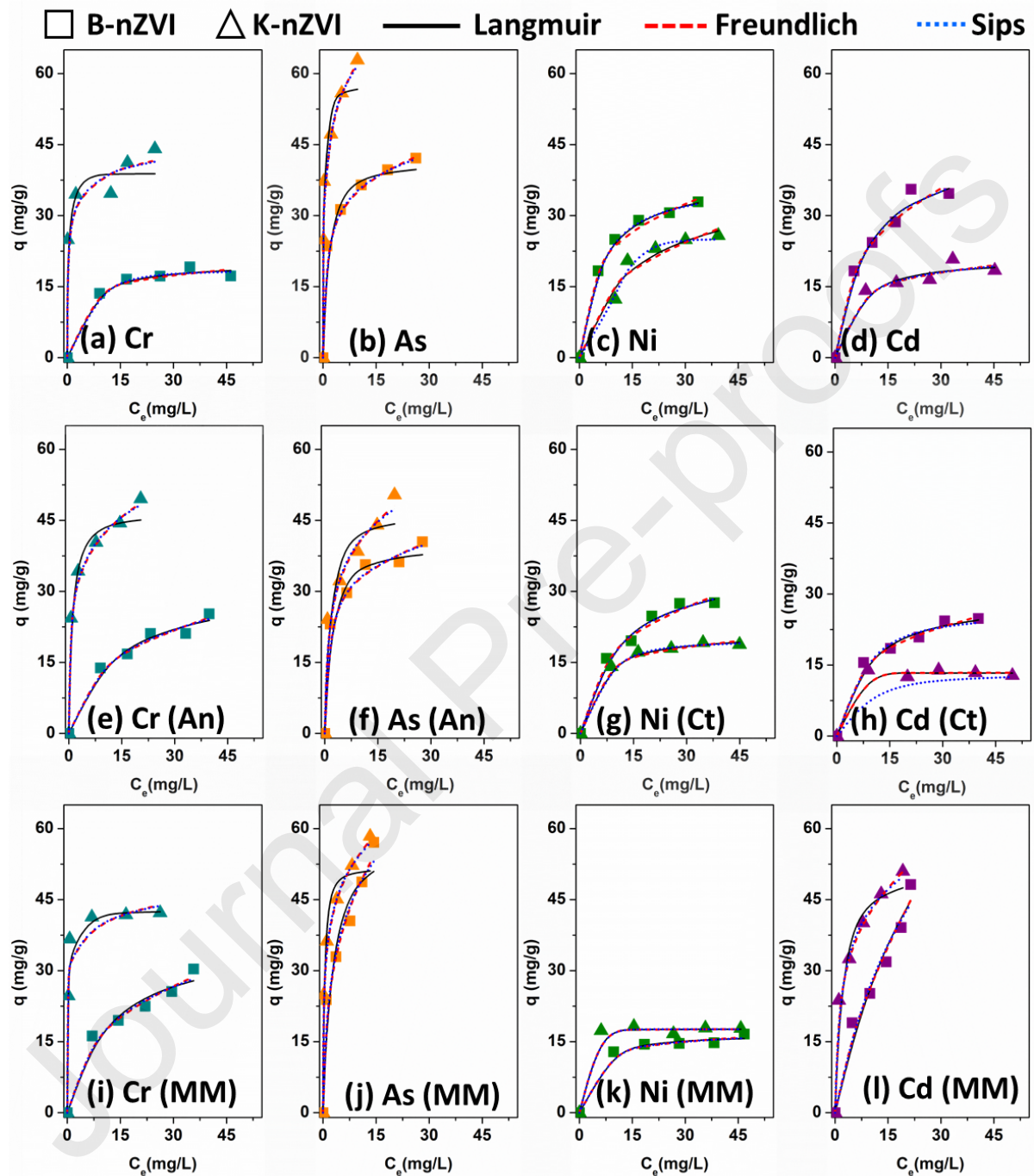


Fig. 7 Impact of varying contaminants concentration on sorption capacity of B-nZVI and K-nZVI composites and sorption isotherm modeling in (a-d) mono-ionic, (e-h) co-ionic and (i-l)

multi-ionic contaminant solutions [$m= 20$ mg, $V= 20$ mL, $C_0= 10-75$ mg/L, $T= 25^\circ\text{C}$, $\text{RPM}= 200$, $\text{pH}= 6.5$, $t= 12\text{h}$]

Similar preferential behavior of B-nZVI and K-nZVI was observed in co-ionic contaminant solutions (fig.7 e-h). While B-nZVI showed a slight increase in sorption capacities for chromium (51.1 mg/g) and arsenic (98.2 mg/g), it was still lower than K-nZVI (126.9 mg/g and 121.3 mg/g, respectively). This may be attributed to enhanced aging of B-nZVI in the presence of co-anionic solutions and suggests co-operative effects of oxy-anions. In contrast, a decrease in respective sorption capacities of Ni^{2+} and Cd^{2+} was observed for both the composites suggesting competitive effects in the presence of metal cations. The simultaneous presence of Cr(III) and As(III) can lead to the formation of ternary complexes leading to their higher sorption capacities. Therefore, total anion sorption capacities were 149.33 mg/g and 248.3 mg/g for B-nZVI and K-nZVI, respectively, which were comparatively higher than the individual chromium and arsenic removal capacities of the composites. Similarly, total cation sorption capacities were 32.9 mg/g (B-nZVI) and 63.4 mg/g (K-nZVI) and were slightly higher than the individual cation sorption capacities of respective composites. This slight increase can be attributed to the impact of enhanced total contaminant load in the system leading to higher sorption on heterogeneous surfaces of composites.

Similarly, the simultaneous presence of both anionic and cationic contaminants led to increased total metal sorption capacities of composites (fig.7 e-l). Obtained parameters from well-fitted Sips isotherm model (table S4c) have shown higher sorption capacities of K-nZVI for anions i.e., chromium (62.2 mg/g and 98.1 mg/g) and arsenic (131.6 mg/g and 169.6 mg/g), respectively for B-nZVI and K-nZVI. In the case of cationic species, B-nZVI showed higher sorption capacities than K-nZVI for both Ni^{2+} (20.1 mg/g and 17.7 mg/g) and Cd^{2+} (113.2 mg/g and 87.1 mg/g). Sorption capacity for cadmium increased drastically of both the composites, compared to mono and co-ionic solutions. Interestingly, total maximum contaminant sorption

capacities of both B-nZVI (327 mg/g) and K-nZVI (372 mg/g) were several folds higher than mono-ionic sorption capacities. A comparison of sorption capacities of earlier reported adsorbents is provided in Table S6 of supplementary information. This behavior can again be attributed to enhanced co-operative effects due to the presence of both cations and oxy-anions in the system that can facilitate multi-layer stacking, ternary complexation, and co-precipitation in the system, leading to enhanced removal of contaminants. Thermodynamic calculations (Table S5) showed that ΔG values were negative in all the cases and mostly < -20 kJ/mol suggesting reaction spontaneity and chemisorption characteristics [59, 60].

3.5 Effect of solution pH

Attributing to the high sorption affinity of B-nZVI for cationic species and K-nZVI for anionic contaminants, similar preferential sorption behavior was observed at varying pH as well (fig. S8 a-l). Therefore, in the studied pH range of 3.5 to 10 K-nZVI showed comparatively higher sorption capacity for chromium and arsenic, whereas B-nZVI showed higher removal of Ni^{2+} and Cd^{2+} in mono-ionic and co-ionic contaminant exposure. A slight decrease in the sorption of anionic species at alkaline pH can be attributed to negative surface charge of both B-nZVI and K-nZVI that led to electrostatic repulsion in the system with anionic contaminant species and unfavorable ligand exchange (OH^-) reactions in basic conditions. For example, As(III) prevails as $\text{As}(\text{OH})_3$ at $\text{pH} < 9$ which behaves like a ligand and can undergo ligand exchange reactions with OH^- on Fe-OH surface sites. This reaction is facilitated on positively charged (i.e. protonated) surface sites (Fe-OH_2^+) because surface H_2O groups are more easily exchanged than OH^- leading to pH-dependent decreasing adsorption of As(III) on composites surface.

In contrast, we observed an increase in the sorption capacity for cationic species with an increase in pH, which may also be attributed to the formation of insoluble metal hydroxide

species at very alkaline conditions (pH=10). Interestingly, in the multi-ionic system, K-nZVI has shown higher sorption of all the contaminants in the studied pH range (3.5-10) that can be attributed to all the cooperative effects as described in previous sections. In the case of a highly acidic environment (pH=3.5), composites have shown a decrease in the sorption capacity for all the contaminants, which may be due to the leaching of formed Fe^{2+} , resulting in slight desorption of contaminants.

3.6 Environmental applications: contaminant preference in complex water matrices

It is a critical challenge for adsorbents to remove the trace amounts of contaminants and to keep the contaminant concentration below the drinking water permissible limit in environmental water samples. The observed variation in the growth behavior of nZVI particles on different clay surfaces that led to their respective preferential behavior and higher sorption capacities for electrostatically favored contaminants allowed further investigation on their behavior in different complex water matrices. For that, four different waters, i.e., synthetic groundwater, synthetic freshwater, synthetic wastewater, and natural river water, were spiked with 10 mg/L of each contaminant (Cr, As, Ni, and Cd) together.

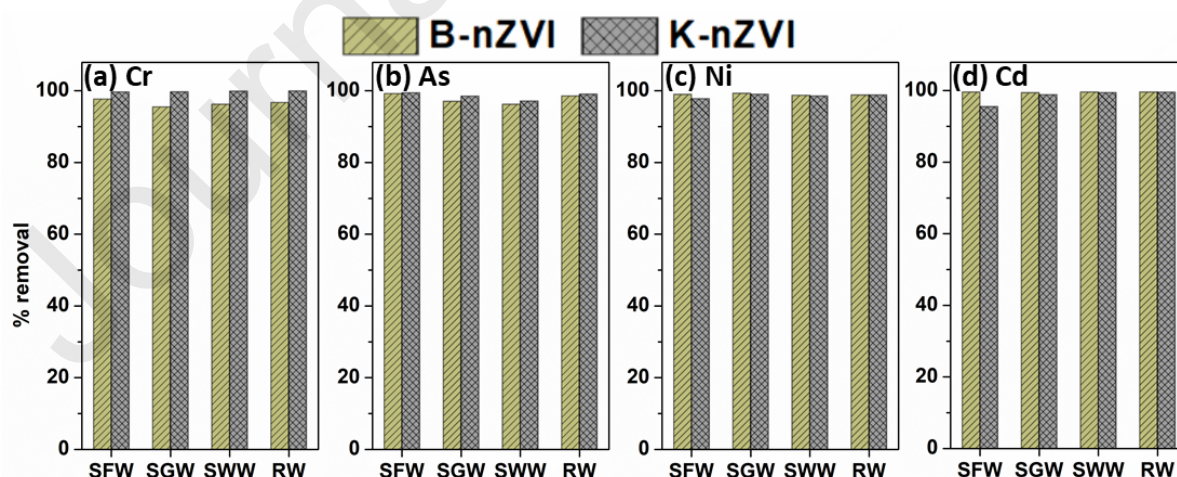


Fig.8 removal of various metallic species from different aqueous matrices [m= 20 mg, V= 20 mL, C_0 = 10 mg/L, T= 25°C, RPM= 200, t= 12h]

Interestingly, results have shown (fig. 8 a-d) that both the composites were able to remove all the contaminants to >98% in all studied water matrices. Observed concentration of different contaminants in various elutes shown that K-nZVI was able to remediate water for chromium and arsenic oxy-anions below permissible limits, whereas B-nZVI succeeded in sequestering Ni^{2+} and Cd^{2+} up to drinking water standards as set by WHO, in all studied types of complex aqueous matrices.

3.7 Environmental applications: secondary iron release

Fe^0 oxidation and secondary release of iron ions and sorbed contaminants is a big challenge for the commercialization of nZVI based solutions for water purification and wastewater treatment. Here, we have monitored iron release during all sorption experiments with both the composites. Results in fig. S9 show that both the composites have prevented iron release below its permissible limit of 2 mg/L. Moreover, the mean values of iron release were 0.012 mg/L for B-nZVI and 0.038 mg/L for K-nZVI. Obtained most extreme outliers were in case of high acidic solutions i.e., pH= 3.5 in both cases. Results confirm that considering preferential sorption of specific ionic species, B-nZVI and K-nZVI can be applied to higher cationic-low anionic contamination and higher anionic-low cationic contamination systems, respectively for sustainable water treatment.

4. Conclusions

The study concludes that varying crystal structures and surface properties of clays lead to different growth behavior of redox-sensitive nZVI particles on these supporting surfaces. Here, swelling bentonite showed Fe^0 nanoparticles growth both in the interlayers and on the surface while only surface attachment was observed in non-swelling kaolinite. Variation in growth behavior altered various surface properties of formed B-nZVI and K-nZVI composites such as nanoparticles size, surface area, zeta potential, etc. These surface variations resulted in

selectively higher sorption of electrostatically favored species on respective composites, i.e., positively charged K-nZVI for chromium and arsenic oxy-anions (87.47 and 157.35 mg/g) than of negatively charged B-nZVI (18.44 and 86.88 mg/g). Oppositely, B-nZVI has shown higher sorption of metal cations Ni^{2+} and Cd^{2+} (36 mg/g and 46 mg/g) than K-nZVI (25 and 27 mg/g). Detailed characterization of reaction precipitates suggested reductive co-precipitation of Cr(VI), complexation of As(III), complexation and co-precipitation of Ni^{2+} and Cd^{2+} with generated iron-oxy—hydroxides were the major contaminant removal mechanisms with co-operative effects in multi-ionic contaminated solutions. Sorption capacities ranged to 327 mg/g and 372 mg/g for B-nZVI and K-nZVI, respectively in multi-contaminant solutions, justifying higher total metal sorption capacities of both composites.

nZVI growth variation on different clay surfaces has also shown a significant implication in drinking water purification and wastewater treatment, where we observed the ability of B-nZVI and K-nZVI to remediate cationic and anionic metal species, respectively, below the WHO-defined maximum permissible limits from freshwater, groundwater, river water and wastewater like complex aqueous matrices. Overall, this study concludes that the -dependent variation in the growth of redox-sensitive nanoparticles can lead to a variation in their surface properties, resulting in variation in selectively higher removal of specific ionic species than others. Designed composites i.e., B-nZVI and K-nZVI can be used to remediate higher metal cations- low oxy-anions and low metal cations- high oxy-anions contaminated water bodies, respectively.

Acknowledgments

Authors would like to acknowledge the financial support from the Ramanujan Fellowship grant (SB/S2/RJN-006/2016) from Department of Science and Technology (DST), India. Central instrumentation facility of the Indian Institute of Science Education and Research Kolkata

should be acknowledged for providing composites characterization instruments (BET, ICP-OES, FESEM, TEM, pXRD, and XRF). Nisha Singh and Nitin Khandelwal also want to acknowledge the IISER-K research fellowships.

Appendix A. Supplementary Information (SI)

Supplementary information associated with this article can be found, in the online version, at-

Journal Pre-proofs

References

- [1] W. UNESCO, The United Nations world water development report 2019: Leaving no one behind, UNESCO Paris, 2019.
- [2] A. Boretti, L. Rosa, Reassessing the projections of the World Water Development Report, *Npj Clean Water* 2 (2019). <https://doi.org/UNSP> 15
10.1038/s41545-019-0039-9.
- [3] H. Ali, E. Khan, I. Ilahi, Environmental Chemistry and Ecotoxicology of Hazardous Heavy Metals: Environmental Persistence, Toxicity, and Bioaccumulation, *J Chem-Ny* 2019 (2019) 6730305. <https://doi.org/10.1155/2019/6730305>.
- [4] R.E. Engler, The Complex Interaction between Marine Debris and Toxic Chemicals in the Ocean, *Environ Sci Technol* 46(22) (2012) 12302-12315. <https://doi.org/10.1021/es3027105>.
- [5] S. Rajeshkumar, X. Li, Bioaccumulation of heavy metals in fish species from the Meiliang Bay, Taihu Lake, China, *Toxicol Rep* 5 (2018) 288-295. <https://doi.org/https://doi.org/10.1016/j.toxrep.2018.01.007>.
- [6] R.J. Reeder, M.A.A. Schoonen, A. Lanzirotti, Metal Speciation and Its Role in Bioaccessibility and Bioavailability, *Reviews in Mineralogy and Geochemistry* 64(1) (2006) 59-113. <https://doi.org/10.2138/rmg.2006.64.3>.
- [7] S.J. Hug, L. Canonica, M. Wegelin, D. Gechter, U. von Gunten, Solar Oxidation and Removal of Arsenic at Circumneutral pH in Iron Containing Waters, *Environ Sci Technol* 35(10) (2001) 2114-2121. <https://doi.org/10.1021/es001551s>.
- [8] Z. Wang, R.T. Bush, L.A. Sullivan, J. Liu, Simultaneous Redox Conversion of Chromium(VI) and Arsenic(III) under Acidic Conditions, *Environ Sci Technol* 47(12) (2013) 6486-6492. <https://doi.org/10.1021/es400547p>.
- [9] Z. Hu, K. Chandran, D. Grasso, B.F. Smets, Effect of Nickel and Cadmium Speciation on Nitrification Inhibition, *Environ Sci Technol* 36(14) (2002) 3074-3078. <https://doi.org/10.1021/es015784a>.
- [10] M.A. Barakat, New trends in removing heavy metals from industrial wastewater, *Arab J Chem* 4(4) (2011) 361-377. <https://doi.org/https://doi.org/10.1016/j.arabjc.2010.07.019>.
- [11] K.R. Reddy, Technical Challenges to In-situ Remediation of Polluted Sites, *Geotechnical and Geological Engineering* 28(3) (2010) 211-221. <https://doi.org/10.1007/s10706-008-9235-y>.
- [12] S. Bolisetty, M. Peydayesh, R. Mezzenga, Sustainable technologies for water purification from heavy metals: review and analysis, *Chem Soc Rev* 48(2) (2019) 463-487. <https://doi.org/10.1039/C8CS00493E>.
- [13] C.C. Azubuike, C.B. Chikere, G.C. Okpokwasili, Bioremediation techniques—classification based on site of application: principles, advantages, limitations and prospects, *World Journal of Microbiology and Biotechnology* 32(11) (2016) 180. <https://doi.org/10.1007/s11274-016-2137-x>.
- [14] N.L. Le, S.P. Nunes, Materials and membrane technologies for water and energy sustainability, *Sustain Mater Techno* 7 (2016) 1-28. <https://doi.org/https://doi.org/10.1016/j.susmat.2016.02.001>.
- [15] S. De Gisi, G. Lofrano, M. Grassi, M. Notarnicola, Characteristics and adsorption capacities of low-cost sorbents for wastewater treatment: A review, *Sustainable Materials and Technologies* 9 (2016) 10-40. <https://doi.org/https://doi.org/10.1016/j.susmat.2016.06.002>.
- [16] N. Khandelwal, E. Tiwari, N. Singh, R. Marsac, T. Schäfer, F.A. Monikh, G.K. Darbha, Impact of long-term storage of various redox-sensitive supported nanocomposites on their application in removal of dyes from wastewater: mechanisms delineation through spectroscopic investigations, *J Hazard Mater* (2020) 123375. <https://doi.org/https://doi.org/10.1016/j.jhazmat.2020.123375>.
- [17] S. Mondal, U. Rana, S. Malik, Reduced Graphene Oxide/Fe₃O₄/Polyaniline Nanostructures as Electrode Materials for an All-Solid-State Hybrid Supercapacitor, *The Journal of Physical Chemistry C* 121(14) (2017) 7573-7583. <https://doi.org/10.1021/acs.jpcc.6b10978>.

- [18] B.P. von der Heyden, A.N. Roychoudhury, Application, Chemical Interaction and Fate of Iron Minerals in Polluted Sediment and Soils, *Curr Pollut Rep* 1(4) (2015) 265-279. <https://doi.org/10.1007/s40726-015-0020-2>.
- [19] Y. Zou, X. Wang, A. Khan, P. Wang, Y. Liu, A. Alsaedi, T. Hayat, X. Wang, Environmental Remediation and Application of Nanoscale Zero-Valent Iron and Its Composites for the Removal of Heavy Metal Ions: A Review, *Environ Sci Technol* 50(14) (2016) 7290-304. <https://doi.org/10.1021/acs.est.6b01897>.
- [20] X. Guan, Y. Sun, H. Qin, J. Li, I.M. Lo, D. He, H. Dong, The limitations of applying zerovalent iron technology in contaminants sequestration and the corresponding countermeasures: the development in zerovalent iron technology in the last two decades (1994-2014), *Water Res* 75 (2015) 224-48. <https://doi.org/10.1016/j.watres.2015.02.034>.
- [21] N. Khandelwal, N. Singh, E. Tiwari, G.K. Darbha, Novel synthesis of a clay supported amorphous aluminum nanocomposite and its application in removal of hexavalent chromium from aqueous solutions, *Rsc Adv* 9(20) (2019) 11160-11169. <https://doi.org/10.1039/C9RA00742C>.
- [22] N. Ezzatahmedi, G.A. Ayoko, G.J. Millar, R. Speight, C. Yan, J.H. Li, S.Z. Li, J.X. Zhu, Y.F. Xi, Clay-supported nanoscale zerovalent iron composite materials for the remediation of contaminated aqueous solutions: A review, *Chemical Engineering Journal* 312 (2017) 336-350. <https://doi.org/10.1016/j.cej.2016.11.154>.
- [23] G. Sposito, N.T. Skipper, R. Sutton, S.-h. Park, A.K. Soper, J.A. Greathouse, Surface geochemistry of the clay minerals, *Proceedings of the National Academy of Sciences* 96(7) (1999) 3358. <https://doi.org/10.1073/pnas.96.7.3358>.
- [24] L.N. Shi, Y.M. Lin, X. Zhang, Z.L. Chen, Synthesis, characterization and kinetics of bentonite supported nZVI for the removal of Cr(VI) from aqueous solution, *Chem Eng J* 171(2) (2011) 612-617. <https://doi.org/10.1016/j.cej.2011.04.038>.
- [25] J. Wang, G.J. Liu, T.F. Li, C.C. Zhou, C.C. Qi, Zero-Valent Iron Nanoparticles (NZVI) Supported by Kaolinite for Cu-II and Ni-II Ion Removal by Adsorption: Kinetics, Thermodynamics, and Mechanism, *Aust J Chem* 68(8) (2015) 1305-1315. <https://doi.org/10.1071/Ch14675>.
- [26] A. Baldermann, S. Kaufhold, R. Dohrmann, C. Baldermann, I. Letofsky-Papst, M. Dietzel, A novel nZVI-bentonite nanocomposite to remove trichloroethene (TCE) from solution, *Chemosphere* 282 (2021) 131018. <https://doi.org/https://doi.org/10.1016/j.chemosphere.2021.131018>.
- [27] L.-n. Shi, Y.-M. Lin, X. Zhang, Z.-l. Chen, Synthesis, characterization and kinetics of bentonite supported nZVI for the removal of Cr(VI) from aqueous solution, *Chem Eng J* 171(2) (2011) 612-617. <https://doi.org/https://doi.org/10.1016/j.cej.2011.04.038>.
- [28] G. Sheng, X. Shao, Y. Li, J. Li, H. Dong, W. Cheng, X. Gao, Y. Huang, Enhanced Removal of Uranium(VI) by Nanoscale Zerovalent Iron Supported on Na-Bentonite and an Investigation of Mechanism, *The Journal of Physical Chemistry A* 118(16) (2014) 2952-2958. <https://doi.org/10.1021/jp412404w>.
- [29] N. Ezzatahmedi, G.A. Ayoko, G.J. Millar, R. Speight, C. Yan, J. Li, S. Li, J. Zhu, Y. Xi, Clay-supported nanoscale zerovalent iron composite materials for the remediation of contaminated aqueous solutions: A review, *Chem Eng J* 312 (2017) 336-350. <https://doi.org/https://doi.org/10.1016/j.cej.2016.11.154>.
- [30] I. Aksu, E. Bazilevskaya, Z.T. Karpyn, Swelling of clay minerals in unconsolidated porous media and its impact on permeability, *GeoResJ* 7 (2015) 1-13. <https://doi.org/https://doi.org/10.1016/j.grj.2015.02.003>.
- [31] C.L.G. Amorim, R.T. Lopes, R.C. Barroso, J.C. Queiroz, D.B. Alves, C.A. Perez, H.R. Schelin, Effect of clay-water interactions on clay swelling by X-ray diffraction, *Nuclear Instruments and Methods in Physics Research Section A: Accelerators, Spectrometers, Detectors and Associated Equipment* 580(1) (2007) 768-770. <https://doi.org/https://doi.org/10.1016/j.nima.2007.05.103>.
- [32] E.M. Araujo, A.M.D. Leite, R.A.d. Paz, V.d.N. Medeiros, T.J.A.d. Melo, H.d.L. Lira, Polyamide 6 Nanocomposites with Inorganic Particles Modified with Three Quaternary Ammonium Salts, 4(11) (2011) 1956-1966.

- [33] Y.-H. Son, J.-K. Lee, Y. Soong, D. Martello, M. Chyu, Structure–Property Correlation in Iron Oxide Nanoparticle–Clay Hybrid Materials, *Chemistry of Materials* 22(7) (2010) 2226-2232. <https://doi.org/10.1021/cm9024843>.
- [34] A. Sachan, D. Penumadu, Identification of Microfabric of Kaolinite Clay Mineral Using X-ray Diffraction Technique, *Geotechnical and Geological Engineering* 25(6) (2007) 603. <https://doi.org/10.1007/s10706-007-9133-8>.
- [35] S. Bae, R.N. Collins, T.D. Waite, K. Hanna, Advances in Surface Passivation of Nanoscale Zerovalent Iron: A Critical Review, *Environ Sci Technol* 52(21) (2018) 12010-12025. <https://doi.org/10.1021/acs.est.8b01734>.
- [36] N. Khandelwal, M.P. Behera, J.K. Rajak, G.K. Darbha, Biochar–nZVI nanocomposite: optimization of grain size and FeO loading, application and removal mechanism of anionic metal species from soft water, hard water and groundwater, *Clean Technol Envir* (2020). <https://doi.org/10.1007/s10098-020-01846-7>.
- [37] F. Huber, D. Schild, T. Vitova, J. Rothe, R. Kirsch, T. Schäfer, U(VI) removal kinetics in presence of synthetic magnetite nanoparticles, *Geochim Cosmochim Acta* 96 (2012) 154-173. <https://doi.org/https://doi.org/10.1016/j.gca.2012.07.019>.
- [38] K. Yotsuji, Y. Tachi, H. Sakuma, K. Kawamura, Effect of interlayer cations on montmorillonite swelling: Comparison between molecular dynamic simulations and experiments, *Appl Clay Sci* 204 (2021) 106034. <https://doi.org/https://doi.org/10.1016/j.clay.2021.106034>.
- [39] F.T. Madsen, M. Müller-Vonmoos, The swelling behaviour of clays, *Appl Clay Sci* 4(2) (1989) 143-156. [https://doi.org/https://doi.org/10.1016/0169-1317\(89\)90005-7](https://doi.org/https://doi.org/10.1016/0169-1317(89)90005-7).
- [40] X. Zhang, S. Lin, Z. Chen, M. Megharaj, R. Naidu, Kaolinite-supported nanoscale zerovalent iron for removal of Pb²⁺ from aqueous solution: Reactivity, characterization and mechanism, *Water Res* 45(11) (2011) 3481-3488. <https://doi.org/https://doi.org/10.1016/j.watres.2011.04.010>.
- [41] L.-n. Shi, X. Zhang, Z.-l. Chen, Removal of Chromium (VI) from wastewater using bentonite-supported nanoscale zerovalent iron, *Water Res* 45(2) (2011) 886-892. <https://doi.org/https://doi.org/10.1016/j.watres.2010.09.025>.
- [42] C. Reginatto, I. Cecchin, K.S. Heineck, K.R. Reddy, A. Thomé, Use of Nanoscale Zero-Valent Iron for Remediation of Clayey Soil Contaminated with Hexavalent Chromium: Batch and Column Tests, *International journal of environmental research and public health* 17(3) (2020). <https://doi.org/10.3390/ijerph17031001>.
- [43] M.M. Tarekegn, A.M. Hiruy, A.H. Dekebo, Nano zero valent iron (nZVI) particles for the removal of heavy metals (Cd²⁺, Cu²⁺ and Pb²⁺) from aqueous solutions, *RSC advances* 11(30) (2021) 18539-18551. <https://doi.org/10.1039/d1ra01427g>.
- [44] Ç. Üzümlü, T. Shahwan, A.E. Eroğlu, K.R. Hallam, T.B. Scott, I. Lieberwirth, Synthesis and characterization of kaolinite-supported zerovalent iron nanoparticles and their application for the removal of aqueous Cu²⁺ and Co²⁺ ions, *Appl Clay Sci* 43(2) (2009) 172-181. <https://doi.org/https://doi.org/10.1016/j.clay.2008.07.030>.
- [45] J. Adusei-Gyamfi, V. Acha, Carriers for nano zerovalent iron (nZVI): synthesis, application and efficiency, *Rsc Adv* 6(93) (2016) 91025-91044. <https://doi.org/10.1039/C6RA16657A>.
- [46] A. Kumar, P. Lingfa, Sodium bentonite and kaolin clays: Comparative study on their FT-IR, XRF, and XRD, *Materials Today: Proceedings* 22 (2020) 737-742. <https://doi.org/https://doi.org/10.1016/j.matpr.2019.10.037>.
- [47] C. Wei-Min, H. Xiang-Ming, Z. Yan-Yun, W. Ming-Yue, H. Zun-Xiang, Y. Xing-Teng, Preparation and swelling properties of poly(acrylic acid-co-acrylamide) composite hydrogels, *E-Polymers* 17(1) (2017) 95-106. <https://doi.org/https://doi.org/10.1515/epoly-2016-0250>.
- [48] A. Liu, W.-x. Zhang, Fine structural features of nanoscale zerovalent iron characterized by spherical aberration corrected scanning transmission electron microscopy (Cs-STEM), *Analyst* 139(18) (2014) 4512-4518. <https://doi.org/10.1039/C4AN00679H>.
- [49] D. Niriella, R. Carnahan, Comparison Study of Zeta Potential Values of Bentonite in Salt Solutions, *J Disper Sci Technol* 27 (2005) 123-131. <https://doi.org/10.1081/DIS-200066860>.

- [50] J.F. Moulder, W.F. Stickle, W.M. Sobol, K.D. Bomben, Handbook of X-Ray Photoelectron Spectroscopy, 1992.
- [51] A. Kraut-Vass, C.J. Powell, S.W. Gaarenstroom, NIST X-ray photoelectron spectroscopy database, Measurement Services Division of the National Institute of Standards and ...2012.
- [52] P. Acharya, Z.J. Nelson, M. Benamara, R.H. Manso, S.I.P. Bakovic, M. Abolhassani, S. Lee, B. Reinhart, J. Chen, L.F. Greenlee, Chemical Structure of Fe–Ni Nanoparticles for Efficient Oxygen Evolution Reaction Electrocatalysis, *Acs Omega* 4(17) (2019) 17209-17222. <https://doi.org/10.1021/acsomega.9b01692>.
- [53] É.C. Lima, M.A. Adebayo, F.M. Machado, Kinetic and Equilibrium Models of Adsorption, in: C.P. Bergmann, F.M. Machado (Eds.), Carbon Nanomaterials as Adsorbents for Environmental and Biological Applications, Springer International Publishing, Cham, 2015, pp. 33-69. https://doi.org/10.1007/978-3-319-18875-1_3.
- [54] L.D.T. Prola, F.M. Machado, C.P. Bergmann, F.E. de Souza, C.R. Gally, E.C. Lima, M.A. Adebayo, S.L.P. Dias, T. Calvete, Adsorption of Direct Blue 53 dye from aqueous solutions by multi-walled carbon nanotubes and activated carbon, *Journal of Environmental Management* 130 (2013) 166-175. <https://doi.org/https://doi.org/10.1016/j.jenvman.2013.09.003>.
- [55] N. Khandelwal, E. Tiwari, N. Singh, R. Marsac, T. Schäfer, F.A. Monikh, G.K. Darbha, Impact of long-term storage of various redox-sensitive supported nanocomposites on their application in removal of dyes from wastewater: Mechanisms delineation through spectroscopic investigations, *J Hazard Mater* 401 (2021) 123375. <https://doi.org/https://doi.org/10.1016/j.jhazmat.2020.123375>.
- [56] H.K. Boparai, M. Joseph, D.M. O'Carroll, Cadmium (Cd²⁺) removal by nano zerovalent iron: surface analysis, effects of solution chemistry and surface complexation modeling, *Environmental Science and Pollution Research* 20(9) (2013) 6210-6221. <https://doi.org/10.1007/s11356-013-1651-8>.
- [57] N. Ayawei, A.N. Ebelegi, D. Wankasi, Modeling and Interpretation of Adsorption Isotherms, *Journal of Chemistry* 2017 (2017) 3039817. <https://doi.org/10.1155/2017/3039817>.
- [58] S.-Y. Woo, H.-S. Lee, J.-S. Kim, K.-H. Kim, H. Ji, Y.-D. Kim, Applicability assessment of functional adsorption zeolite materials in adsorption desalination cum cooling systems driven by low-grade heat source, *Chemical Engineering Journal* 430 (2022) 131375. <https://doi.org/https://doi.org/10.1016/j.cej.2021.131375>.
- [59] S. Raghav, D. Kumar, Adsorption Equilibrium, Kinetics, and Thermodynamic Studies of Fluoride Adsorbed by Tetrametallic Oxide Adsorbent, *Journal of Chemical & Engineering Data* 63(5) (2018) 1682-1697. <https://doi.org/10.1021/acs.jced.8b00024>.
- [60] Y. Cantu, A. Remes, A. Reyna, D. Martinez, J. Villarreal, H. Ramos, S. Trevino, C. Tamez, A. Martinez, T. Eubanks, J.G. Parsons, Thermodynamics, Kinetics, and Activation energy Studies of the sorption of chromium(III) and chromium(VI) to a Mn(3)O(4) nanomaterial, *Chem Eng J* 254 (2014) 374-383. <https://doi.org/10.1016/j.cej.2014.05.110>.